Nuclear Instruments and Methods in Physics Research A306 (1991) 366–377
North-Holland

# Performance of a balloon-borne magnet spectrometer for cosmic ray studies

R.L. Golden, C. Grimani, R. Hull, B.L. Kimbell, R. Park, S.A. Stephens, S. Stochaj and W.R. Webber
*New Mexico State University, Particle Astrophysics Laboratory, Las Cruces, NM 88003-0001, USA*

G. Basini, E. Bonaviri, F. Massimo Brancaccio and M. Ricci
*Laboratori Nazionali INFN, Italy*

J.F. Ormes, E.S. Seo and R.E. Streitmatter
*NASA/Goddard Space Flight Center, USA*

F. Celletti and P. Spillantini
*Università di Firenze, Firenze, Italy*

A. Codino, M. Menichelli and I. Salvatori
*Università di Perugia, Perugia, Italy*

F. Bongiorno
*Università di Roma I (La Sapienza), Roma, Italy*

V. Bidoli, A. Buccheri, M.P. De Pascale, A. Morselli and P. Picozza
*Università Tor Vergata, Italy*

Received 2 January 1991

This paper summarizes the performance characteristics of the balloon-borne magnet spectrometer operated by New Mexico State University's Particle Astrophysics Laboratory. Particular emphasis has been placed on the rigidity resolution, including both random and systematic errors of the magnetic spectrometer system. Measurement of the performance characteristics has been greatly enhanced through the use of an imaging calorimeter as an independent aid in the identification of cosmic rays.

## 1. Introduction

The balloon-borne magnet spectrometer discussed in this paper has been in operation since 1976. During this time it was used in 1976 to measure proton, helium, electron and positron spectra (see for example refs. [1–4]), in 1979 and 1986 to observe antiprotons [3,5], and in 1989 to observe antiprotons, deuterium, electrons, positrons and helium-3 (results are in preparation). The instrument was also used in 1988 by a team from Goddard Space Flight Center to search for low energy antiprotons [6].

A description of the spectrometer as used in the 1976 flight was published in ref. [7]. The system has had numerous improvements since that time. During the preparations for the 1989 campaign, an extensive ground exposure of the instrument was made using more than 100 000 sea level muons. The inclusion of an imaging calorimeter in the detector array, increased computing capabilities and improved data analysis techniques, have

0168-9002/91/$03.50 

enabled a significantly more detailed study of the spectrometer performance. In this paper we provide details of the analysis procedures. We also report the observed and simulated resolution functions including random and systematic errors.

The results presented here have been used in the analysis of data from the recent balloon flights [6,8,9]. They were also used to check that events with large spurious curvature were not responsible for the observation of antiprotons as reported by Golden et al. in ref. [5] (hereafter referred to as "the 1979 flight").

## 2. Instrument description

Fig. 1 shows the NMSU balloon-borne magnet spectrometer in the configuration used for the 1989 balloon flight campaign. The spectrometer includes eight multiwire proportional counters (MWPC) in the high-field region of a superconducting magnet. The other detectors in the instrument are time-of-flight detectors (two layers above and two layers below the spectrometer), a gas Cherenkov detector with a threshold Lorentz factor of 23, and an imaging calorimeter 6.4 radiation lengths deep. The instrument is triggered by a 4-fold coincidence between the time-of-flight (TOF) detectors. Both pulse-height and timing information were obtained from the TOF counters.

The gas Cherenkov detector, G, utilizes about 1 m of Freon 12–Freon 22 mixture (50–50) as the active medium. Light is focused on 4 RCA S83006E 5 in. phototubes using a mirror made of four segments of 1/16 in. black polystyrene plastic. The mirror segments are vacuum-formed to spherical shape and front-surface coated with aluminum and magnesium fluoride. Pulse heights from each tube are measured for every event. The average response for a fully relativistic singly charged particle is 10–12 photoelectrons. Details of the Cherenkov detector performance appear in a separate publication [10]. S1 is a scintillator designed for high resolution pulse-height measurements.

The tracking system multiwire proportional counters (MWPC) used delay-line readout. All eight of the MWPCs are equipped for measurement on the axis with maximum deflection ($x$-axis, see figs. 1 and 2) and four of the MWPCs have $y$-axis readouts. The MWPC are arranged with a pair of chambers at the top, middle and bottom of the spectrometer. In addition there is a single chamber at the 1/4 height and another at the 3/4 height locations in the spectrometer. The 4 $y$-readout chambers are located at the bottom, middle, 3/4, and top of the spectrometer. Further details of the MWPCs may be found in [11].

The magnet is shown to the left of the MWPC stack in fig. 1. It is a single coil of 11 161 turns of copper-clad NbTi wire. The outer diameter of the coil is 24 in. The

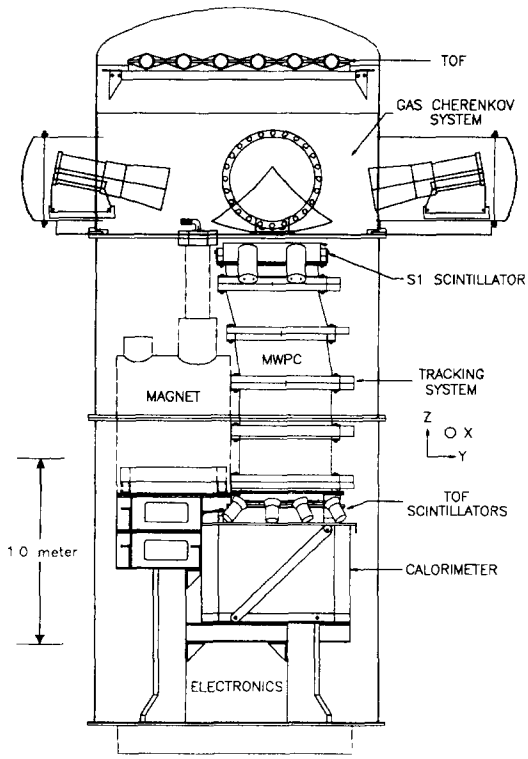


Fig. 1. The instrument configuration. Note the origin and orientation of the coordinate system.

coil's radial thickness is 5 in. and the axial thickness is 3 in.

The imaging calorimeter is shown at the bottom of the detector stack in fig. 1. It is composed of 21 layers each composed of 64 streamer tubes on the $x$-axis and 64 tubes on the $y$-axis. The calorimeter includes integral

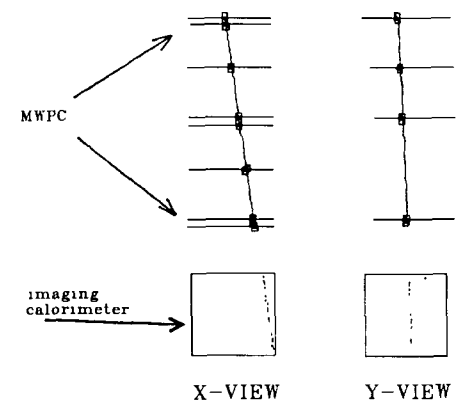


Fig. 2. A reconstructed event. This event is a 5.9 GV muon observed during the ground-level run in Price Albert, Sask. The Cherenkov detector indicated the presence of 15.6 photoelectrons. Note that the $x$ view is on the left and the $y$ view is on the right.

readout electronics built from custom hybrid electronic circuits.

### 3. Track reconstruction and spectrometer alignment

The determination of the particle rigidity begins with the transformation of raw MWPC data into measured track coordinates in a 3-D coordinate system. When a particle transverses an MWPC, the avalanche in the MWPC causes pulses to be injected into delay lines. The times of arrival are measured for the MWPC pulses at each end of the delay line. For a particular delay line we will designate the two time values at $t_a$ and $t_b$ The "raw position estimate" for chamber $i$ is then

$$(x_{\text{raw}})_i = \frac{\bar{v}(t_a - t_b)_i}{2}, \tag{1}$$

where $\bar{v}$ is the average pulse propagation velocity with a similar expression used for the $y$-axis.

The sum $(t_a + t_b)$ should be equal to the total delay for each delay line. Testing this sum can eliminate multiple tracks or cases where either or both ends of the delay line fail to have digitized the time. Before using MWPC data, each sum is tested and required to be within the equivalent of $\sim 1$ cm of the total line length.

In order to be used in data analysis an event is usually required to have five good $x$ time sums and three good $y$ time sums. In addition each of the pairs of chambers at the top, middle and bottom of the stack must have at least one chamber with a good time sum. Finally, the bottom $y$ time sum is required to be good. These tests assure that spurious tracks are not allowed into the analysis procedure.

The delay lines used in the readout process have small position-dependent changes in their propagation velocities. This gives rise to position dependant nonlinear errors. In the case of the $x$-axis these nonlinearities were removed by a correction table but currently they are removed by a harmonic expansion whose parameters are determined for each flight. This linearizing process has the form

$$(x_{\text{lin}})_i = a_i(x_{\text{raw}})_i + \sum_{j=1}^{4}\left[b_{ji}\cos\left(\frac{\pi(x_{\text{raw}})_i}{L}j\right) + c_{ji}\sin\left(\frac{\pi(x_{\text{raw}})_i}{L}j\right)\right], \tag{2}$$

where

$a_i$ = scale factor for measurement $i$,
$b_{ji}$ = the $j$th harmonic cosine coefficient for chamber $i$,
$c_{ji}$ = the $j$th harmonic sine coefficient for chamber $i$,
$L$ = the length of a chamber (50 cm).

The $y$-axis, having a lower resolution, is corrected using a table of measured errors which is allowed only an adjustable scale factor

$$(y_{\text{lin}})_i = d_i T_i(y_{\text{raw}}), \tag{3}$$

where $T_i$ represents the tabular correction for delay line $i$ and $d_i$ is the scale factor for delay line $i$.

The linearized position measurement is transformed into a 3-D coordinate value by three rotations followed by a 3-D translation. Using small-angle approximations, we have

$$\begin{aligned}(X_{\text{rotat}})_i &= (x_{\text{lin}})_i - (\theta_z)_i(y_{\text{lin}})_i,\\ (Y_{\text{rotat}})_i &= (\theta_z)_i(y_{\text{lin}})_i + (\theta_z)_i(x_{\text{lin}})_i,\\ (Z_{\text{rotat}})_i &= -(\theta_y)_i(x_{\text{lin}})_i + (\theta_y)_i(y_{\text{lin}})_i,\end{aligned} \tag{4}$$

where $(\theta_x)_i$, $(\theta_y)_i$, $(\theta_z)_i$ represents the three rotation angles for chamber $i$. The translation is of the form

$$\begin{aligned}(X_{\text{meas}})_i &= (X_{\text{rotat}})_i + (x_0)_i,\\ (Y_{\text{meas}})_i &= (Y_{\text{rotat}})_i + (y_0)_i,\\ (Z_{\text{meas}})_i &= (Z_{\text{rotat}})_i + (z_0)_i,\end{aligned} \tag{5}$$

where $(x_0)_i$, $(y_0)_i$, $(z_0)_i$ represent the translation of chamber $i$s origin to the payload coordinate system.

The constants for chamber i used in the track reconstruction are $a_i$, $b_{ji}$, $c_{ji}$, $d_i$, $\theta_{xi}$, $\theta_{yi}$, $\theta_{zi}$ and $x_{0i}$, $y_{0i}$, $z_{0i}$. This is a total of 16 parameters. Thus for eight chambers there are 128 parameters. Not all of these parameters need be determined. For example, one chamber's origin can be chosen as the origin of the coordinate system. Another chamber's location with respect to the origin is chosen to define local vertical, and some chambers do not need the $y$-axis scale factor. These constraints still leave 118 parameters which must be determined. The determination is made by operating the spectrometer with the magnet off. With the magnet off, the measured trajectories are straight lines except for Coulomb scattering and measurement errors. An ensemble of events is then recorded and used as a set of straight-line geodesics for the alignment procedure. To start the procedure, an initial guess is taken for the rotations and translations and the delay-line linearization constants are set to zero. A subset of events which appears reasonably straight is then selected (they are fitted to a straight line hypothesis). This subset is used as input to a multiparameter minimizing program. The program varies the rotations and translations to minimize the overall chi-square for the chosen subset of straight tracks.

Once the program has converged, the set of alignment constants is adopted as an intermediate solution. A new subset of events is chosen from the ensemble using slightly stricter straightness criteria. This new subset is then used in conjunction with the minimizer to obtain a refined set of alignment constants. The selection and refinement cycle is repeated until a self-consistent subset of events and alignment constants evolves. This normally takes only three or four iterations.

When the alignment constants have been determined they are held fixed while the minimizing program varies the delay-line linearity constants. Normally the mini-

mizing program is allowed to co-linearize each of the bottom, middle and top pairs separately. Then the remaining two chambers are linearized.

When both the alignment constants and the linearity constants have been determined, the *entire* process is repeated using these constants as the starting point.

The total alignment process takes about 1 day of interactive computing time, it converges quickly and the second run through the process serves to verify the stability of the result. As a final cross-check, the resulting alignment and linearity parameters are used to momentum-analyze the entire straight-track data set. The resulting distribution of curvatures serves as the resolution function for the instrument.

In subsequent sections we discuss the momentum analysis process and the performance of the spectrometer once it has been aligned.

## 4. Track fitting

The track fitting process uses an iterative least-squares procedure developed by Solmitz and Burkhardt [12]. In this procedure a particle's "state" is described by the $X$ and $Y$ coordinates at $Z = 0.0$, two direction tangents ($dx/dz$ and $dy/dz$) at $Z = 0.0$, and the particle's magnetic deflection $\eta$. The magnetic deflection is defined as $\eta = Ze/pc$, where $Ze$ is the particle charge and $p$ is the particle's momentum, and $c$ is the speed of light. The units normally used are $GV^{-1}$. We will often refer to $\eta$ as simply "the deflection". An initial guess at the state is made by using data from the top and bottom MWPCs plus the assumption that the deflection is zero. Then a trajectory is computed by stepwise integration of the equations of motion. Appendix A provides the details of the trajectory computation.

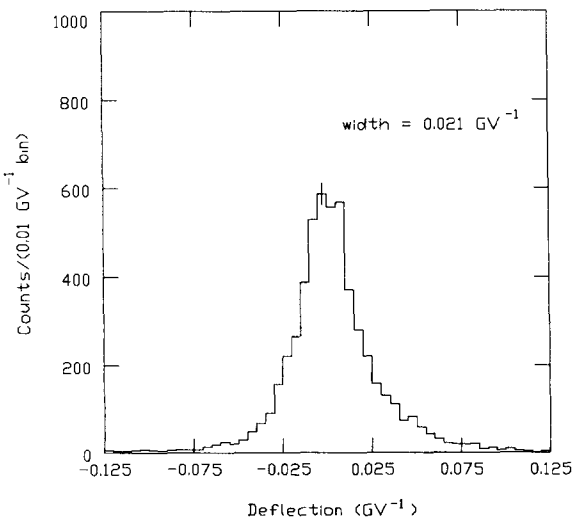


Fig. 3. Deflection distributions for events with Cherenkov counter on. No requirements were placed on the calorimeter data. The root-mean-square width is 0.021 $GV^{-1}$.

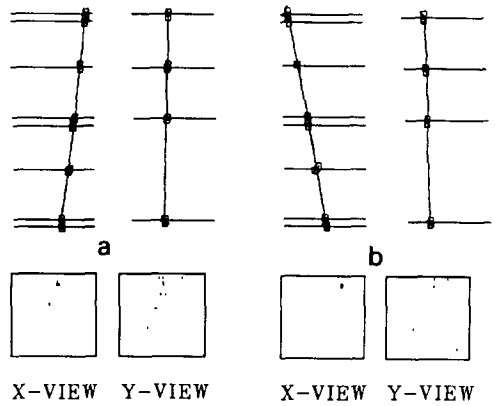


Fig. 4. Calorimeter images for two events with large deflection. Event (a) had an apparent deflection of −0.14 GV. Event (b) had an apparent deflection of −0.20 GV. Both events were accompanied by a large number of photoelectrons in the appropriate portion of the Cherenkov detector.

Appendix B describes how a revised state vector, corresponding to a better fit to the trajectory, can be calculated given an initial, approximate trajectory. The revised state vector is used as the basis for yet another computed trajectory. This process is repeated until the state vector stabilizes. Each new state is compared with the previous state vector. The iteration is stopped when the position values change less than 10 μm, the angles change less than 0.1 mrad and the deflection changes less than 0.003 $GV^{-1}$.

Once the least-squares process has converged, the last calculated trajectory is compared to the measured coordinates and chi-squares are computed for both the $X$ and $Y$ coordinates:

$$\chi_x^2 = \sum_{\substack{i \\ \text{(chambers)}}} \left( \frac{(x_{\text{fit}}) - (x_{\text{meas}})}{\sigma_{xi}} \right)^2, \tag{6}$$

$$\chi_y^2 = \sum_{\substack{i \\ \text{(chambers)}}} \left( \frac{(y_{\text{fit}}) - (y_{\text{meas}})}{\sigma_{yi}} \right)^2. \tag{7}$$

## 5. Observed performance

As mentioned in the previous section, data taken while the magnet is off should yield MWPC trajectories that appear straight except for Coulomb scattering and measurement errors. At low energies (less than a GeV or so) the Coulomb scattering error becomes significant. Since there are such particles in the sea-level radiation, this effect contributes strongly to the presence of events

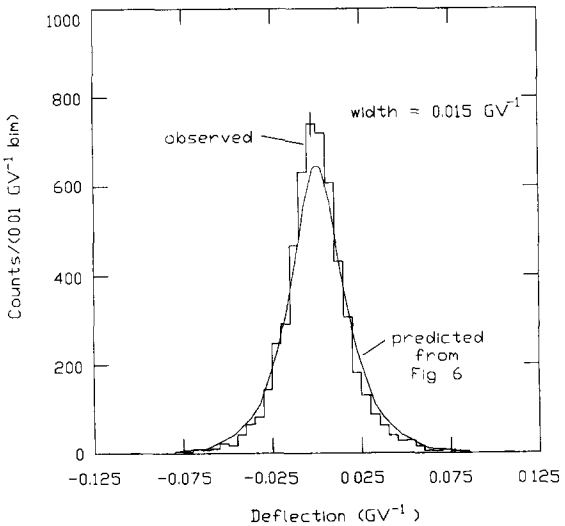


Fig. 5 Deflection distribution of events having the Cherenkov detector on and having a single track penetrate the calorimeter. The smooth curve results from a convolution of Gaussians whose rms width distribution is given in fig. 6.

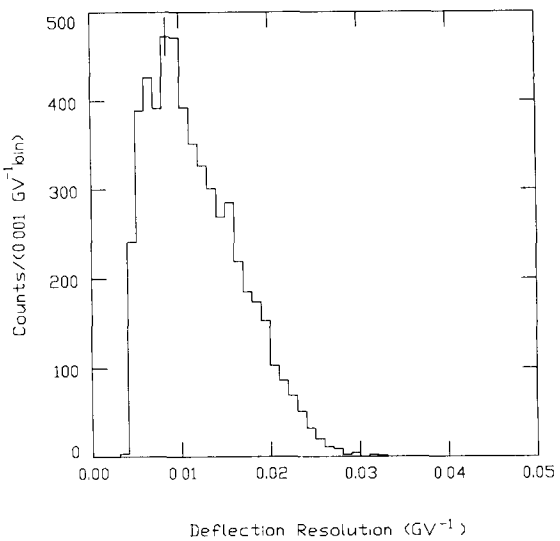


Fig. 6. Distribution of computed deflection resolutions values. Note that the peak is at 0.0085 GV$^{-1}$. This indicates that the most probable resolution uncertainty corresponds to the deflection of a 118 GV particle.

with large apparent deflections. If one requires that the particle be accompanied by Cherenkov light then low energy muons are eliminated (but not low energy electrons).

A sample of 100 000 magnet-off events was gathered on August 12, 1990 at Prince Albert, Saskatchewan. A sample of events which should be high-energy muons was selected from this run using the following criteria:

1) at least 5 X MWPC coordinates pass the sum test;
2) at least 3 Y MWPC coordinates pass the sum test;
3) the MWPC data indicates that the track will exit the bottom of the calorimeter;
4) the Cherenkov detector indicates at least one photoelectron

Fig. 2 shows the reconstruction of a typical event from the August 12 sample. The squares are the measurements transferred to the 3-D coordinate system. The lines through the squares represent the fitted trajectory. Note the image in the calorimeter. It is typical for a single muon traversal.

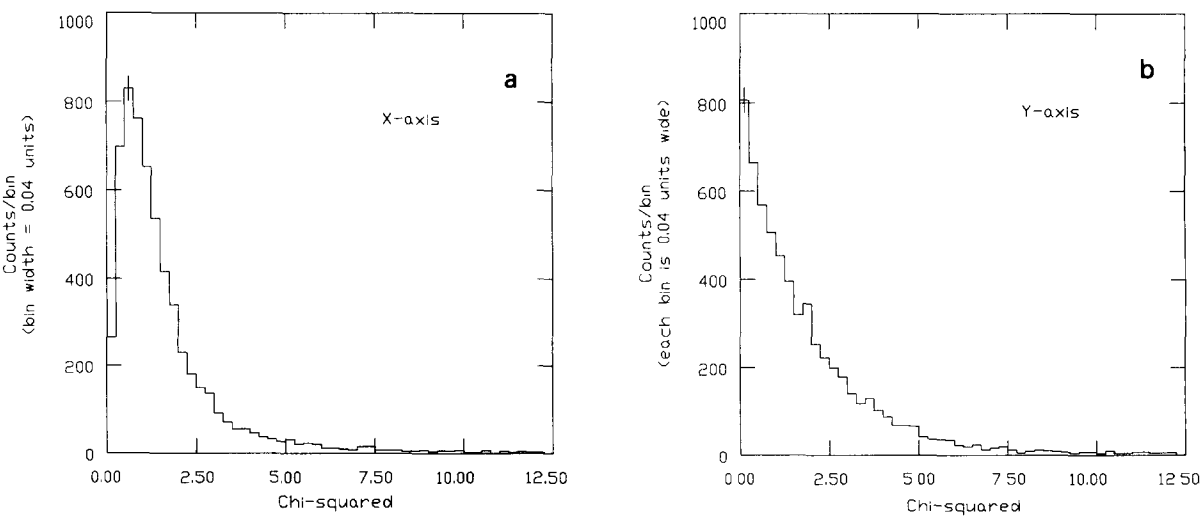


Fig. 7. Chi-squared distributions for events having the Cherenkov detector on and having a single track penetrating the calorimeter. Note that normally events are required to have chi-squared less than 5.0 for the $x$-axis and 7.5 for the $y$-axis.

Fig. 3 shows the deflection distribution for these events. This figure shows the presence of a small number of events with very large deflections. Figs. 4a and 4b show the calorimeter images for two typical events with large deflections. The pattern is indicative of a low energy electron and accompanying soft photons. An examination of *all* of the large deflection events shows that *none* of them have a clean, single track traversing the calorimeter. If we add the requirement that the particles penetrate the calorimeter without cascading, electrons of all energies are eliminated. We add the following two criteria to eliminate what we believe is the low energy electron component:

5) the calorimeter must contain a single track that has at least 10 of the 21 planes fired in the $x$ view;
6) the calorimeter track corresponds within 0.5 cm of the extrapolated MWPC track.

Fig. 5 shows the deflection distribution of a set of events selected with criteria 1–6. As long as Coulomb scattering is not significant, measurements of a set of particles all having the same rigidity can be expected to yield a deflection distribution with a shape given by fig. 5. Thus, this distribution can be regarded as the resolution function for the instrument.

Fig. 6 is a histogram of the deflection uncertainty as determined during the fitting process. This computed quantity is $\sigma_\eta = 1/(\partial\chi^2/\partial\eta^2)^{1/2}$. Appendix B explains how this quantity is computed. Events with large uncertainties are found to result from trajectories that traversed the lower field regions of the spectrometer, or had a small number of usable MWPC measurements. If one performs a convolution of the distribution in fig. 6 with Gaussian distributions of the corresponding widths, one should obtain the curve in fig. 5. The smooth curve in fig. 5 is the result of such a convolution. The excellent correspondence indicates that the computed resolution for each event is indeed a good estimator for an individual particle's deflection uncertainty. The computation for $\sigma_\eta$ (given in appendix B) shows that $\sigma_\eta$ depends on the assigned measurement errors. Thus, the correspondence is valid only if the correct measurement errors are used in the fitting program.

The chi-square distributions are shown in figs. 7a and 7b. These distributions have been normalized by dividing them by the degrees of freedom. The assumed MWPC resolutions range from 180 to 270 μm. Their determination is discussed further in the next section.

## 6. Simulated performance

The performance of the spectrometer has also been studied using Monte Carlo techniques. The simulation program uses the following steps:

1) a random particle state vector is generated;
2) the trajectory is determined by stepwise integration of the equations of motion. This process can include, at the users option, Coulomb and nuclear scattering;
3) measurement errors are then introduced to the calculated trajectory;
4) the resulting simulated measurements are then analyzed using the same technique as for real data;
5) steps 1–4 are repeated to generate an ensemble of simulated events.

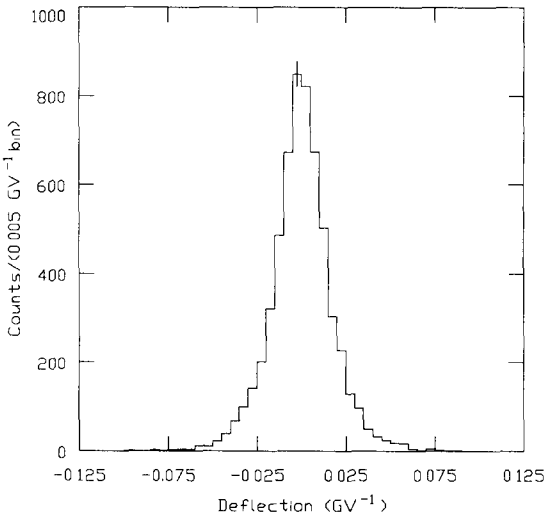


Fig. 8. Deflection distribution generated by Monte Carlo The rms width of this distribution is 0.015 GV$^{-1}$, the same as observed in the measured events.

The Monte Carlo program was adjusted so that the chi distributions for each of the MWPC matched between simulation and observation. The resulting $x$ resolutions ranged from 180 to 270 μm. The $y$ resolutions ranged from 600 to 1200 μm. Once the MWPC resolutions were matched, the Monte Carlo program was used to produce expected deflection distributions, and chi-squared distributions. Figs. 8, 9a and 9b are Monte Carlo results corresponding to observed data in figs. 5, 7a and 7b. Nuclear scattering was not included in this computation since the particles observed are predominantly muons. It was necessary to include Coulomb scattering to obtain a match between the simulation and observation. Although the muons have a mean energy of about 5 GeV, Coulomb scattering contributes significantly to the tail of the distribution in fig. 8. As can be seen, the simulated deflection distribution and chi-square distributions agree well with the observed distributions. The Monte Carlo calculation of the deflection resolutions was also found to be in excellent agreement with that in fig. 6.

### 6.1. Coulomb scattering

The material in the MWPC system consists of the material in the eight MWPCs plus the gas in the spaces

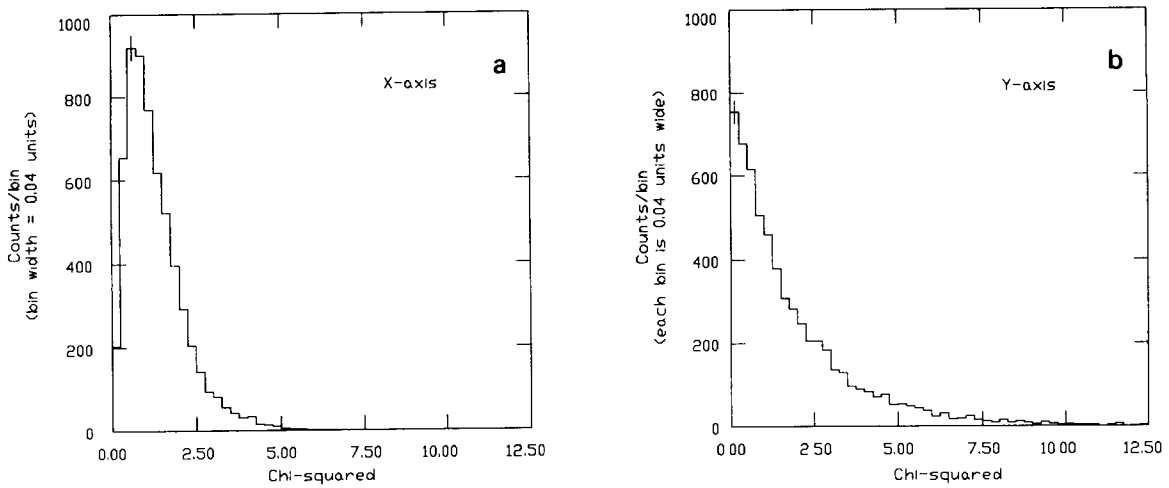


Fig. 9. Chi-square distribution for Monte Carlo events. These figures should be compared to the observed chi-square distributions in figs. 7a and 7b.

between the MWPCs. The gas was normally dry nitrogen but was a 50–50 mixture of Freon 12 and Freon 22 in the 1979 flight. The total interchamber gas thickness was 105 cm. Each MWPC had two 0.001 in. thick mylar windows and two 0.001 in. thick Kynar windows. The chambers were 2.5 cm thick and were filled with "Magic Gas" (mostly argon). There were two grids of 100 μm diameter stainless-steel wires. There were 256 wires in each grid. There was also a single 256-wire grid of 25 μm diameter stainless-steel wires. The total MWPC assembly had 0.008 radiation lengths of material when the Freon mixture was used between the chambers. Fig. 10 contains the deflection distribution generated for Coulomb scattering effects on 1 GV muons. The measurement error contributions have been set to zero in this distribution. In general, Coulomb scattering is expected to be of the form $(\Delta\eta/\eta)(\alpha/\beta)$. In fig. 10 we find an $\Delta\eta_{coul} = 0.037\ GV^{-1}$ for 1 GV muons. We thus conclude that for this instrument the Coulomb scattering induced deflection uncertainty is of the form,

$$\Delta\eta_{coul} = 0.037\eta/\beta, \tag{8}$$

where

$\eta$ = deflection,

$\beta$ = velocity/$c$.

This error should add in quadrature to other uncertainties in the measured deflection.

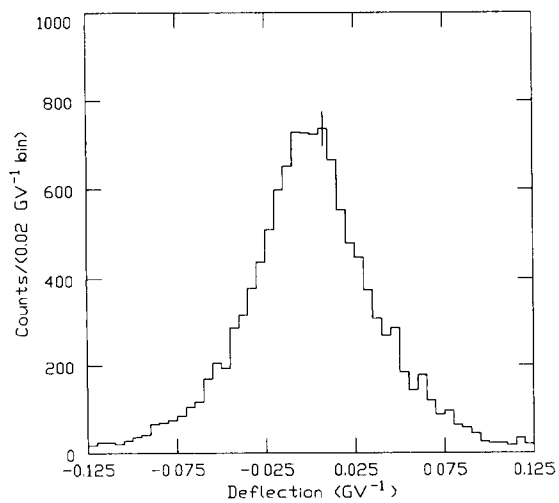


Fig. 10. Deflection distribution for 1 GV muons. Measurement errors are not included in this distribution. The rms of this distribution is 0.037 $GV^{-1}$.

### 6.2. Nuclear scattering

Protons traversing the spectrometer can undergo nuclear scattering. If the scatter produces secondaries, the event will be rejected because the MWPC sum test will fail when multiple particles are present. Scatters that have only a small number of short range secondaries or no secondaries (coherent proton–nucleus scatters) can pass the normal selection criteria. It is of interest to know if the scattering of positive protons can produce apparent antiproton events. Belletini et al. [13] provide the differential cross sections for proton–nucleus scattering. These cross sections have been incorporated in the Monte Carlo simulations. A detailed analysis of the effects of nuclear scattering is contained in [14]. We present a summary here. The total interaction mean free path for proton–carbon elastic scattering is 250 g/cm$^2$. The total amount of material in the spectrometer depends strongly on the molecular weight of the gas between the MWPC. The worst case is the 1979 flight in which this space was filled with a 50–50 mixture of Freon 12 and Freon 22. For that flight the

material is equivalent to 0.44 g/cm$^2$ of carbon. Thus the odds of a scatter for any particular proton traversal are $1.8 \times 10^{-3}$. In the 1979 flight this implies that there were 150 scatters. The elastic scatters result from coherent nuclear scatters or quasi-elastic scatters. Coherent nuclear scatters are ones in which the proton interacts with the targets as a whole. Quasi-elastic scatters are ones where the proton scatters from an individual target nucleon. This usually results in a recoil particle which would result in a bad MWPC time sum, but we have kept both types of interactions in our background calculations. The cross section for these scatters is

$$\frac{d\sigma}{d\Omega} = (72e^{-61t} + 5e^{-10t}) \text{ b/sr}, \quad (9)$$

where $t = (p_t)^2$ ($p_t$ = transverse momentum in GeV).

The first term represents the coherent scattering. It contributes 71% of the scatters. The mean scattering angle is about the same as the magnetic deflection angle of a 10 GeV particle. The second term represents the quasi-elastic scatters (29% of the total number of scatters) and has an average scattering angle about twice that of the magnetic deflection angle of a 10 GeV proton. For any particular scatter to give rise to a spurious negative curvature event, the scatter must occur near the middle of the spectrometer, be mostly in the plane of magnetic curvature, be in the direction to change the sign of the charge, be of large enough amplitude to change the apparent sign of charge, and not appear as a "kink"[ (i.e. it must fit as a smooth curve).

Fig. 11 shows the distribution of 1500 nuclear scatter events generated by the Monte Carlo technique. This is equivalent to 10 times the number of scatters expected during the 1979 flight. These particles were all 10 GeV protons. Simulations at both 20 and 5 GeV showed that the fraction of "spillover" protons was slightly less at those energies. Measurement errors and Coulomb scattering errors were also included in the simulation. Events in this distribution were selected to typical chi-square selection criteria. We find that the number of scatters in the region $-0.2$ to $-0.08$ GV$^{-1}$ is 35, giving rise to an expectation of 3.5 nuclear scatter background events during that flight. Normally events used for antiproton observations are also required to have a curvature that is more than 5 standard deviations from zero. This requirement reduces the expected nuclear scatter background to 1.8 events. Later flights of this instrument used air or nitrogen as the medium between the MWPC chambers. This reduces the expected background by a factor of 2.

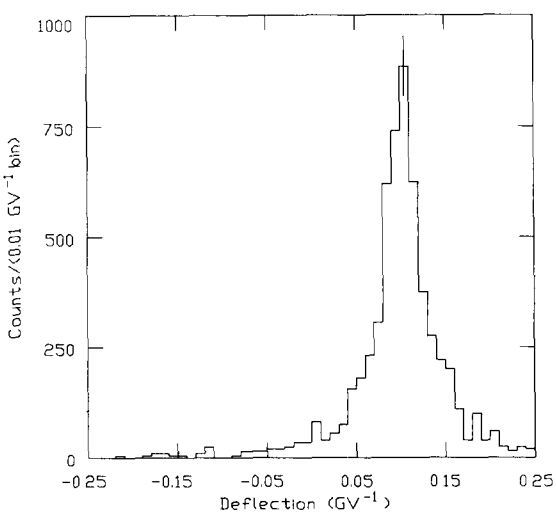


Fig. 11. The deflection distribution of 1500 10 GV protons which have undergone a coherent nuclear scatter. This is the equivalent of 10 times the number of scatters in the 1979 balloon flight.

## 7. Antiproton observations and antihelium searches

Antiproton observations and searches for antihelium require good understanding of the instrument resolution and, if possible, elimination of events with positive charge appearing with spurious negative deflection. One simple step is to require that each event have a reasonably small deflection uncertainty. As mentioned earlier, and detailed in appendix B, the deflection uncertainty is computed for each event. Events with a large uncertainty are typically due to having traversed a low amount of magnetic field or may be missing some MWPC data. Inspection of the $\sigma_\eta$ distribution reveals that the majority of events have an uncertainty less that 0.03 GV$^{-1}$. Events with uncertainty greater than 0.03 GV$^{-1}$ should not be utilized for antiproton or antihelium experiments.

Since the deflection uncertainty $\sigma_\eta$ is computed for each event, it is also possible to require that each event have a statistically significant curvature. If one requires that $|\eta|/\sigma_\eta$ be large than one can be assured that the sign of a particle's charge is reliably determined. One can evaluate what values of $|\eta|/\sigma_\eta$ are required to eliminate events with spurious negative curvature by Monte Carlo methods. For example one can assume a spectrum of positive nuclei, then convolve this distribution using Gaussians whose widths are given by the deflection uncertainties (see fig. 5). Such a Monte Carlo results in a tail of events with spurious negative curvatures. One can determine the number of expected background events for a particular set of upper limits on $\sigma_\eta$ and $|\eta|/\sigma_\eta$ by imposing these restrictions on the Monte Carlo events. The restriction on $\sigma_\eta$ is normally determined by inspection of events with large $\sigma_\eta$. As $\sigma_\eta$ increases one usually finds a point beyond which character of the events clearly changes and only events with

low numbers of measured coordinates and low magnetic field traversed are found. Once a $\sigma_\eta$ limit is determined, the limit on $|\eta|/\sigma_\eta$ can be set by the Monte Carlo studies. Though the limits vary from experiment to experiment, restrictions of $\sigma_\eta < (0.025$ to $0.04)$ and $|\eta|/\sigma_\eta > (5$ or $6)$ give background limits of much less than 1 false sign-of-charge per flight.

## 8. Efficiencies

It is often desirable to measure and report absolute fluxes of various species of particles (e.g. fluxes in units of particles/cm$^2$sr s GV). This requires, among other things, determination of the efficiency for particles passing each of the selection criteria used in selecting the particles. Typical selection criteria relating to the spectrometer are to require that:

1) at least five $x$ measurements have good time sums;
2) at least three $y$ measurements have good time sums;
3) at least one good $x$ time sum be found for each of the top, middle and bottom chamber pairs;
4) the bottom $y$ chamber have a good time sum;
5) the iterative least squares fitting procedure converge in less than nine iterations;
6) the $x$ chi-square be less than 5 and the $y$ chi-square be less than 7.5.

Criteria 1–6 represent the "normal" selection criteria. Often "strict" criteria are used where criteria 1 and 2 are changed to require that eight good $x$ and four good $y$ time sums be found.

Events are digitized when a coincidence is found between the entrance and exit scintillator arrays. About half of the triggers are due to events with side showers or other false coincidences (i.e. many tracks with large zenith angles or no tracks at all). Prior to 1986 there was no onboard computer and all triggers were digitized and recorded. Since 1986, a computer in a payload gathers data from all triggers but requires that at least four $x$ chambers be fired in order to place the event in the transmission queue. A small fraction of the data (1–3% depending on the flight) is transmitted without this additional requirement.

The remaining triggers are normally accompanied by a single incident vertical track. Multiple vertical track events are also observed as are events with tracks that are outside the trigger geometry but still caused a trigger (probably due to an unseen second track). It is of interest to know what the probability is for a bonafide particle passing through the spectrometer to pass the above criteria. Such an event can fail the above criteria in numerous ways: 1) interactions causing multiple tracks, 2) failure of MWPCs to register the ionization of the particle, 3) traversal of an insensitive region of an MWPC (there are a few broken anode wires that have been removed) etc. Because of these failure modes there are strong correlations observed in the performance of adjacent MWPCs and between the two axes of a single MWPC. Since the MWPC responses are correlated, it is difficult to determine the overall efficiency from the individual efficiencies. It is best to utilize an independent ensemble of test events which are known to have a single good track. In the early experiments (1975–1979), the instrument incorporated nine scintillators (two to define the entrance geometry and seven as part of a shower counter at the exit). These scintillators were arranged so that their geometric factor was slightly more restrictive that the acceptance geometry of the spectrometer. To measure the efficiency of the spectrometer system, events were selected in which all nine scintillators indicated a $Z = 1$ particle. These events were then used as the test ensemble for the spectrometer. The efficiencies for passing the above criteria were measured on many occasions during ground runs and flight preparations. Typically, the efficiencies were around 60%. Temporal variations were negligible over periods of weeks. Efficiency measurements made on the ground and during flight were found to be in good agreement. But significant variations (5–10%) were noticed when the experiment was reconfigured (e.g. disassembled and reassembled). It is believed that the changes in efficiency were due to changes in the electronic noise in the instrument and settings for the constant fraction discriminators used in the delay line timing circuits. It should also be noted that the efficiency depends strongly on variations in the criteria used to test the spectrometer data.

In the 1989 ground test data, the imaging calorimeter can be used as an independent track recognition device. A program was devised to find events with a single track in the calorimeter, and a consistent single-track signature in the scintillator data. These events were further tested, using the calorimeter track, to assure that they went through the MWPC geometry. Finally, for these events, we required that the Cherenkov detector indicate that the particle was relativistic. Events thus chosen, represent a sample of single-track events chosen independent of the MWPC data (except for the payload computer test that four $x$ chambers be fired). Using the 1989 ground-run data, we find that $0.70 \pm 0.01$ of the events chosen by the calorimeter method pass selection criteria 1–6 listed above. If one changes to the strict criteria, then $0.55 \pm 0.01$ of the events pass. In order to see if the four $x$ chamber test imposed by the payload computer had biased the result, we repeated the efficiency measurement using the events which passed the calorimeter tests but had not been tested by the flight computer. The efficiency for passing criteria 1–6 was found to be $0.68 \pm 0.08$. The uncertainty is much larger due to the decreased statistics but no bias is observed.

During the flight, the test was repeated. Unfor-

tunately the single track efficiency in the calorimeter declined during the flight (due to a gas leak in the calorimeter). Due to the decreased efficiency it was not possible to use software to select and fit calorimeter data. Instead, the events not subjected to the payload computer test for four $x$ chambers fired were examined individually. A sample of 131 events was identified that had a useable, calorimeter selected track. The efficiency using these events was found to be $0.56 \pm 0.07$ for the "strict" version of criteria 1–6. This is in good agreement with the ground data.

## 9. Conclusion

The performance of the NMSU balloon-borne magnet spectrometer can be fully understood using a straightforward model for its performance. Over the years it has consistently performed with resolutions exceeding 100 GV. The resolution function for the instrument can be understood as a convolution of Gaussians whose widths are related to the numbers of measured coordinates and amounts of magnetic field traversed by the particles under study. Studies of the effects of small-angle nuclear scatters show that these events contribute at most a few events background to typical observations. A detailed study of the resolution function shows that a simple selection procedure can be used to reduce the number of spurious events with the incorrect sign-of-charge to less than 1 in $10^5$.

## Acknowledgements

This work was supported by NASA Grants NAGW-110, NAGW-1418 and the Italian National Institute of Nuclear Physics (INFN).

## Appendix A

*Track reconstruction in nonuniform fields*

The magnetic field in the instrument is not easily represented as an analytic function. In order to facilitate reconstruction of particle trajectories, the field table was generated using numerical integration of the Biot–Savart equation. This field table was then used as part of a stepwise integration of a particle's trajectory through the magnetic field. A particle's state vector can be described by five parameters: $(x_1, y_1, (\mathrm{d}x/\mathrm{d}z)_1, (\mathrm{d}y/\mathrm{d}z)_1, \eta)$, where the subscript 1 denotes MWPC no. 1, the reference of the coordinate system, and $\eta$ is the particle's magnetic deflection. Given these parameters one can calculate the location of the particle as it traversed other MWPCs.

The equation of motion for a particle of charge $q$ and mass $m$ in a magnetic field $\boldsymbol{B}$ is

$$\gamma m \frac{\mathrm{d}^2 \boldsymbol{r}}{\mathrm{d}t^2} = \frac{q}{c}\left(\frac{\mathrm{d}\boldsymbol{r}}{\mathrm{d}t} \times \boldsymbol{B}\right).$$

If we define the path length as $l = \beta ct$ and use the relation $\eta = q/\gamma\beta mc$, we have

$$\frac{\mathrm{d}^2 \boldsymbol{r}}{\mathrm{d}l^2} = \frac{q}{\gamma\beta mc^2}\frac{\mathrm{d}\boldsymbol{r}}{\mathrm{d}l} \times \boldsymbol{B} = \frac{\eta}{c}\left(\frac{\mathrm{d}\boldsymbol{r}}{\mathrm{d}l} \times \boldsymbol{B}\right). \tag{A.1}$$

One can then treat the stepwise integration of the particle's trajectory as follows: The new "slope" after a step $\Delta l$ can be estimated as

$$\left(\frac{\mathrm{d}\boldsymbol{r}}{\mathrm{d}l}\right)' = \frac{\mathrm{d}\boldsymbol{r}}{\mathrm{d}l} + \frac{\mathrm{d}^2 \boldsymbol{r}}{\mathrm{d}l^2}\Delta l, \tag{A.2}$$

where $\mathrm{d}^2\bar{r}/\mathrm{d}l^2$ is given by eq. (A.1).
The new position can be estimated as

$$\boldsymbol{r}' = \boldsymbol{r} + \frac{1}{2}\left(\frac{\mathrm{d}\boldsymbol{r}'}{\mathrm{d}l} + \frac{\mathrm{d}\boldsymbol{r}}{\mathrm{d}l}\right)\Delta l. \tag{A.3}$$

The averaging of $\mathrm{d}\boldsymbol{r}/\mathrm{d}l$ in eq. (A.3) is particularly important. It assures that successive integration of the second order equations of motion do not generate any first order accumulated errors.

## Appendix B

*Iterative least-squares solution to the equations of motion*

We will chose a specific MWPC (denoted by a subcript 1) as the plane in which we define a particles state vector

$$\boldsymbol{\alpha} = \left(x_1, y_1, \left(\frac{\mathrm{d}x}{\mathrm{d}z}\right)_1, \left(\frac{\mathrm{d}y}{\mathrm{d}z}\right)_1, \eta\right),$$

where $\eta$ is the particle's magnetic deflection. The state vector serves as a set of initial conditions for integrating the equations of motion. Given the state vector, the particles trajectory though the remaining MWPCs can be calculated by integrating the equations of motion (see appendix A). For a particular calculated trajectory we can obtain a set of calculated chamber coordinates $(x_i, y_i)$. The $\chi^2$ for this calculated trajectory is then

$$\chi^2 = \sum_{\substack{i \\ \text{(planes)}}} \left(\frac{x_i - x_{\mathrm{m}i}}{\sigma_{xi}}\right)^2 + \left(\frac{y_i - y_{\mathrm{m}i}}{\sigma_{yi}}\right)^2, \tag{B.1}$$

where $x_{\mathrm{m}i}$ and $y_{\mathrm{m}i}$ represent the measured locations in chamber $i$.

Since $x_i$ and $y_i$ are determined by $\boldsymbol{\alpha}$, $\chi^2$ can be regarded as a function of $\boldsymbol{\alpha}$. If $\chi^2$ has been evaluated

for a particular value $\boldsymbol{\alpha}_0$, $\chi^2$ at nearby values can be determined by Taylor series expansion (to second order)

$$\chi^2(\boldsymbol{\alpha}) = \chi^2(\boldsymbol{\alpha}_0) + \left[\sum_j \left(\frac{\mathrm{d}\chi^2}{\mathrm{d}\alpha_j}\right)_{\boldsymbol{\alpha}_0} \Delta\alpha_j + \frac{1}{2}\sum_{jk}\left(\frac{\mathrm{d}^2\chi^2}{\mathrm{d}\alpha_j\,\mathrm{d}\alpha_k}\right)_{\boldsymbol{\alpha}_0}\right]\Delta\alpha_j\,\Delta\alpha_k. \quad \text{(B.2)}$$

Now we wish to take a step $\boldsymbol{\alpha}_0 \to \boldsymbol{\alpha}$ such that $\chi^2$ is minimized. We need then $\partial\chi^2/\partial\alpha_l = 0\,\forall\, l$.
From eq. (B.2) we have

$$\frac{\partial\chi^2}{\partial\alpha_l} = 0 = 0 + \sum_j \left(\frac{\partial\chi^2}{\partial\alpha_j}\right)_{\boldsymbol{\alpha}_0}\frac{\partial\Delta\alpha_j}{\partial\alpha_l} + \frac{1}{2}\sum_{jk}\left(\frac{\partial^2\chi^2}{\partial\alpha_j\partial\alpha_k}\right)_{\boldsymbol{\alpha}_0}\frac{\partial}{\partial\alpha_l}(\Delta\alpha_j\,\Delta\alpha_k). \quad \text{(B.3)}$$

By straightforward differentiation we obtain

$$\frac{\partial\Delta\alpha_j}{\partial\alpha_l} = \delta_{jl},$$

$$\frac{\partial}{\partial\alpha_l}(\Delta\alpha_j\,\Delta\alpha_k) = (\Delta\alpha_j\delta_{jl} + \Delta\alpha_k\delta_{jk}). \quad \text{(B.4)}$$

Combining eqs. (B.3) and (B.4) gives

$$\sum_j \left(\frac{\partial\chi^2}{\partial\alpha_j}\right)_{\boldsymbol{\alpha}_0}\delta_{jl} + \frac{1}{2}\sum_{jk}\left(\frac{\partial^2\chi^2}{\partial\alpha_j\partial\alpha_k}\right)_{\boldsymbol{\alpha}_0}(\Delta\alpha_j\delta_{jl} + \Delta\alpha_k\delta_{kl}) = 0,$$

which reduces to

$$\left(\frac{\partial\chi^2}{\partial\alpha_l}\right)_{\boldsymbol{\alpha}_0} + \sum_j \frac{\partial^2\chi^2}{\partial\alpha_j\partial\alpha_l}\,\Delta\alpha_l = 0. \quad \text{(B.5)}$$

If we define

$$(\boldsymbol{V})_l \equiv \left(\frac{\partial^2\chi^2}{\partial\alpha_l}\right)_{\boldsymbol{\alpha}_0}, \quad (\underset{\sim}{\boldsymbol{Z}})_{jl} \equiv \left(\frac{\partial^2\chi^2}{\partial\alpha_j\partial\alpha_l}\right)_{\boldsymbol{\alpha}_0}, \quad \text{(B.6)}$$

then eq. (B.5) becomes

$$\boldsymbol{V} + \underset{\sim}{\boldsymbol{Z}}(\boldsymbol{\alpha} - \boldsymbol{\alpha}_0) = 0$$

so an estimate for the best fit $\boldsymbol{\alpha}$ can be obtained as

$$\boldsymbol{\alpha} = \underset{\sim}{\boldsymbol{Z}}^{-1}\boldsymbol{V} + \boldsymbol{\alpha}_0. \quad \text{(B.7)}$$

This process of estimating the $\boldsymbol{\alpha}$ that gives the lowest $\chi^2$ is repeated until the desired degree of convergence is obtained. In our case we require that the terms in $\Delta\boldsymbol{\alpha}$ correspond to less than 0.1 mrad, 10 μm and 1/300 GV. The first guess for $\boldsymbol{\alpha}$ is taken by using a straight line fit to the measured coordinates. Convergence is normally reached in three iterations. If a fit takes more than nine iterations the event is regarded as unfittable.

The calculation of $\underset{\sim}{\boldsymbol{Z}}$ and $\boldsymbol{V}$ is now summarized.

Table 1
Partial derivatives of chamber coordinates

| $l$ | $\alpha_l$ | $\frac{\partial x_k}{\partial\alpha_l}$ | $\frac{\partial y_k}{\partial\alpha_l}$ |
|---|---|---|---|
| 1 | $x_1$ | 1 | 0 |
| 2 | $y_1$ | 0 | 1 |
| 3 | $\tan\theta_x$ | $z_k - z_1$ | 0 |
| 4 | $\tan\theta_y$ | 0 | $z_k - z_1$ |
| 5 | $\eta$ | $\frac{x_k - [\alpha_1 + \alpha_3(z_k - z_1)]}{\alpha_5}$ | $\frac{y_k - [\alpha_2 + \alpha_4(z_k - z_1)]}{\alpha_5}$ |

From eqs. (B.5) and (B.1) we have

$$(\boldsymbol{V})_l = \frac{\partial^2\chi^2}{\partial\alpha_l} = 2\left[\sum_{l\,(\text{planes})}\left(\frac{x_l - x_{ml}}{\sigma_{xl}^2}\right)\frac{\partial x_l}{\partial\alpha_l} + \sum_{l\,(\text{planes})}\left(\frac{y_l - y_{ml}}{\sigma_{yl}^2}\right)\frac{\partial y_l}{\partial\alpha_l}\right]. \quad \text{(B.8)}$$

The differentials $\partial x_l/\partial\alpha_l$, $\partial y_l/\partial\alpha_l$ can be approximated as shown in table 1.

The approximations in table 1 are derived from the definitions of $\alpha$'s. For example to calculate $\partial x_k/\partial\alpha_1$ we use

$$x_k \simeq x_1 + \tan\theta_x(z_k - z_1),$$
$$x_k \simeq \alpha_1 + \alpha_3(z_k - z_1), \quad \text{(B.9)}$$
$$\frac{\partial x_k}{\partial\alpha_1} = 1.$$

By similar methods we find $\partial x_k/\partial\alpha_2 = 0$, $\partial y_k/\partial\alpha_1 = 0$, $\partial y_k/\partial\alpha_2 = 1$.

The terms $\alpha_3$ and $\alpha_4$ represent $\cos\theta_x$ and $\cos\theta_y$, respectively. We have, for example,

$$\alpha_3 = \frac{(x_k - x_1)}{(z_k - z_1)}$$

or

$$x_k = \alpha_3(z_k - z_1) + x_1, \quad \text{(B.10)}$$

so

$$\frac{\partial x_k}{\partial\alpha_3} = (z_k - z_1).$$

Similarly we find $\partial x_k/\partial\alpha_4 = 0$, $\partial y_k/\partial\alpha_3 = 0$, $\partial y_k/\partial\alpha_4 = (z_k - z_1)$.
Finally to calculate partials with respect to $\alpha_5$ we use

$$\frac{\partial x_k}{\partial\alpha_5} \simeq \frac{\Delta x_k}{\Delta\alpha_5} = \frac{x_k - x_{ks}}{\alpha_5 - \alpha_{5s}}$$

where $x_{kS}$ is the value of $x_k$ obtained for a straight line fit

$$x_{ks} = x_1 + \tan\theta_x(z_k - z_1) = \alpha_1 + \alpha_3(z_k - z_1).$$

Since a straight line corresponds to $\alpha_5 = 0$ we have $\alpha_{5s} = 0$ and

$$\frac{\partial x_k}{\partial \alpha_5} = \frac{x_k - [\alpha_1 + \alpha_3(z_k - z_1)]}{\alpha_5}. \tag{B.11}$$

Similarly we have

$$\frac{\partial y_k}{\partial \alpha_5} = \frac{y_k - [\alpha_2 + \alpha_4(z_k - z)]}{\alpha_5}. \tag{B.12}$$

The matrix $\boldsymbol{Z}$ is calculated by similar methods. From eq. (6) we have

$$\begin{aligned}(\underset{\sim}{Z})_{lm} &= \frac{\partial x^2}{\partial \alpha_l \partial \alpha_m} = \frac{\partial V_l}{\partial \alpha_m} \\ &= \frac{\partial x^2}{\partial \alpha_l \partial \alpha_m} = \frac{\partial V_l}{\partial \alpha_m} \\ &= 2\left[\sum_{\substack{i \\ \text{(planes)}}} \frac{1}{\sigma_{xi}^2}\left(\frac{\partial x_i}{\partial \alpha_m}\frac{\partial x_i}{\partial \alpha_l} + (x_i - x_{mi})\frac{\partial_{xi}^2}{\partial \alpha_l \partial \alpha_m}\right)\right] \\ &\quad + 2\left[\sum_{\substack{i \\ \text{(planes)}}} \frac{1}{\sigma_{yi}^2}\left(\frac{\partial x_i}{\partial \alpha_m}\frac{\partial x_i}{\partial \alpha_l}\right.\right. \\ &\quad \left.\left. + (x_i - x_{mi})\frac{\partial_{yi}^2}{\partial \alpha_l \partial \alpha_m}\right)\right]. \end{aligned} \tag{B.13}$$

Dropping the second derivative terms we obtain an expression for $\underset{\sim}{Z}$ in terms of the quantities given in table 1.

## References


[1] G.D. Badhwar, R.R. Daniel, T. Cleghorn, R.L. Golden, J.L. Lacy, S.A. Stephens and J.E. Zipse, Proc. 15th Int. Cosmic Ray Conf., Plovdiv 1 (1977) 404.

[2] G.D. Badhwar, R.R. Daniel, T. Cleghorn, R.L. Golden, J.L. Lacy, S.A. Stephens and J.E. Zipse, Proc. 15 Int. Cosmic Ray Conf., Plovdiv 2 (1977) 204.

[3] R.L. Golden, B.G. Mauger, S. Nunn and S. Horan, Astrophys. J. Lett. 24 (1984) 75.

[4] R.L. Golden, S.A. Stephens, B.G. Mauger, G.D. Badhwar, R.R. Daniel, S. Horan, J.L. Lacy and J.E. Zipse, Astron. Astrophys. 188 (1987) 145.

[5] R.L. Golden, S. Horan, B.G. Mauger, G.D. Badhwar, J.L. Lacy, S.A. Stephens, R.R. Daniel and J.E. Zipse, Phys. Rev. Lett. 43 (1979) 1264.

[6] R.E. Streitmatter, S.J. Stochaj, J.F. Ormes, R.L. Golden, S.A. Stephens, T. Bowen, A. Moats and J. Lloyd-Evans, Adv. Space Res. 12 (1989) 65.

[7] R.L. Golden, G.D. Badhwar, J.L. Lacy and J.E. Zipse, Nucl. Instr. and Meth. 148 (1978) 179.

[8] R.L. Golden, S.A. Stephens, Streitmatter, R.E., Stochaj, S.J., Ormes, T. Bowen, A. Moats, J. Lloyd-Evans, PAL preprint no. 67, available on request, submitted to Astrophys. J. Lett. (1990).

[9] E.S. Seo et al., Proc. 22nd Int. Cosmic Ray Conf., Adelaide 3 (1990) 7.

[10] R.L. Golden et al., PAL technical note no. 224, available on request, to be submitted to Nucl. Instr. and Meth. (1990).

[11] J.L. Lacy and R.S. Lindsey, Nucl. Instr. and Meth. 119 (1974) 483.

[12] F. Solmitz and J. Burkhardt, private communication (1969).

[13] Belletini et al., Nucl. Phys. 79 (1966) 609.

[14] R.L. Golden, PAL technical note no. 170 (1980) available on request.